

Elsevier Editorial System(tm) for International Journal of Rock Mechanics and Mining
Sciences

Manuscript Draft

Manuscript Number:

Title: Seismic velocity and Q anisotropy in fractured poroelastic media

Article Type: Paper

Keywords: Fractures,
poroelasticity
anisotropy
velocity dispersion, attenuation
finite elements.

Corresponding Author: Prof. Juan Enrique Santos, PhD

Corresponding Author's Institution: Purdue University

First Author: Juan E Santos, PhD

Order of Authors: Juan E Santos, PhD; Robiel Martinez Corredor; Jose M Carcione, Dr.

West Lafayette, May 3rd 2013

Professor Robert Zimmerman
Editor-in-Chief, International Journal of Rock Mechanics and Mining Sciences

Dear Professor Zimmerman:

I am submitting my paper **Seismic velocity and Q anisotropy in fractured poroelastic material**, by Juan E. Santos, Robiel Martínez Corredor and José M. Carcione to be consider for publication in International Journal of Rock Mechanics and Mining Sciences.

Sincerely

Professor Juan Enrique Santos
Department of Mathematics
Purdue University
150 North University Street
West Lafayette, Indiana, 47907-2067
e-mail: santos@math.purdue.edu

We model fractures in fluid-saturated poroelastic materials

We analyze fracture induced velocity and Q anisotropy

We use the finite element method to model heterogeneous fractured poroelastic materials

Seismic velocity and Q anisotropy in fractured poroelastic media

Juan E. Santos^{a,b,c,*} Robiel Martinez Corredor^d
José M. Carcione^e

^a*CONICET, Instituto del Gas y del Petróleo, Facultad de Ingeniería, Universidad de Buenos Aires, Av. Las Heras 2214 Piso 3 C1127AAR Buenos Aires, Argentina.*

^b*Universidad Nacional de La Plata, La Plata, Argentina.*

^c*Department of Mathematics, Purdue University, 150 N. University Street, West Lafayette, Indiana, 47907-2067, USA.*

^d*Facultad de Ingeniería, Universidad Nacional de La Plata, Argentina.*

^e*Istituto Nazionale di Oceanografia e di Geofisica Sperimentale (OGS), Borgo Grotta Gigante 42c, 34010 Sgonico, Trieste, Italy.*

* Corresponding author. Phone: 541145143026.
E-mail address: santos@math.purdue.edu (J. E. Santos).

Abstract

A fluid-saturated poroelastic isotropic medium with aligned fractures behaves as a transversely isotropic and viscoelastic (TIV) medium when the predominant wavelength is much larger than the average distance between fractures. A planar fracture embedded in a fluid saturated poroelastic background medium can be modeled as a extremely thin and compliant porous layer. P-waves traveling in this type of medium induce fluid-pressure gradients at fractures and mesoscopic-scale heterogeneities, generating fluid flow and slow (diffusion) Biot waves, causing attenuation and dispersion of the fast modes (mesoscopic loss). A poroelastic medium with embedded aligned fractures exhibits significant attenuation and dispersion effects due to this mechanism, which can properly be represented at the macroscale with an equivalent TIV medium. In this work, we apply a set of compressibility and shear harmonic finite-element (FE) experiments on fractured highly heterogeneous poroelastic samples to determine the five complex and frequency dependent stiffnesses characterizing the equivalent medium. The experiments consider brine or patchy brine-CO₂ saturated samples and a brine saturated sample with an heterogeneous (fractal) skeleton with fractures. We show that fractures induces strong seismic velocity and Q anisotropy, both for qP and qSV waves, enhanced either by patchy saturation or frame heterogeneity.

Keywords: Fractures, poroelasticity, anisotropy, velocity dispersion, attenuation, finite elements.

1 Introduction

Seismic wave propagation through fractures is an important subject in hydrocarbon exploration geophysics, mining and reservoir characterization and production [1]. In particular, naturally fractured reservoirs have received interest in recent years, since, generally, natural fractures control the permeability of the reservoir. In geophysical prospecting and reservoir development, knowledge of fracture orientation, densities and sizes is essential since these factors control hydrocarbon production [2,3]. This is also important in CO₂ storage in geological formations to monitor the injected plumes as faults and fractures are generated, where CO₂ can leak to the surface [4]. Among papers presenting numerical approaches to determine effective media corresponding to fractured rocks, Grechka and Kachanov [5,6] performed 3D static FE simulations, summing up the individual contributions of the fractures and ignoring their interactions. Also, Saenger et al. [7] presented numerical simulations in 2D and 3D media saturated with fluids to analyze Biot's predictions in the high and low frequency limits of poroelasticity, while Wenzlau et al. [8] per-

formed FE simulations to analyze anisotropic dispersion and attenuation in poroelastic materials.

A dense set of horizontal fractures in a fluid-saturated poroelastic medium behaves as a TIV medium when the average fracture distance is much smaller than the predominant wavelength of the traveling waves. This leads to frequency and angular variations of velocity and attenuation of seismic waves. A major cause of attenuation in porous media is wave-induced fluid flow, which can take place at mesoscopic-scale heterogeneities, when the fast P-wave is converted into diffusion-type Biot slow waves. Wave anelasticity and anisotropy are significant in fractured poroelastic rocks due to this mechanism [9].

White et al. [10] were the first to introduce the mesoscopic-loss mechanism in the framework of Biot theory considering porous and thin plane layers. Next, Gelinsky and Shapiro [11] obtained the relaxed and unrelaxed stiffnesses of the equivalent poro-viscoelastic medium to a finely layered horizontally homogeneous material. Krzikalla and Müller [12] combined the two previous models assuming that fluid flow is perpendicular to the layering plane and independent of the loading direction; they obtained the five complex and frequency-dependent stiffnesses of the equivalent TIV medium [13].

A planar fracture embedded in a fluid-saturated poroelastic background is a particular case of the thin layer problem, when one of the layers is very thin and compliant. FE harmonic compressibility and shear tests were first presented in [15] to obtain a viscoelastic medium long-wavelength equivalent to a highly heterogeneous isotropic sample. Then, in [14], [16] and [13] the procedure was extended to determine long-wave equivalent media to finely layered viscoelastic and poroelastic materials. The procedure used here was validated using the analytical solution presented in [12] and [9].

In this work, we apply these harmonic FE harmonic tests to saturated isotropic poroelastic samples having a dense set of horizontal fractures modeled as very thin layers. The samples contained mesoscopic-scale heterogeneities due to patchy brine-CO₂ saturation and fractal porosity and consequently, fractal permeability and frame properties. We analyze attenuation and velocity dispersion as function of frequency and propagation angle.

2 The Biot model, equivalent medium and seismic properties

Let us consider isotropic fluid-saturated poroelastic layers and let $\mathbf{u}^s(\mathbf{x}) = (u_1^s, u_2^s, u_3^s)$ and $\mathbf{u}^f(\mathbf{x}) = (u_1^f, u_2^f, u_3^f)$ indicate the time Fourier transform of the displacement vector of the solid and fluid relative to the solid frame,

respectively. Here, if \mathbf{U}^f denotes the fluid displacement vector, $\mathbf{u}^f = \phi(\mathbf{U}^f - \mathbf{u}^s)$, where ϕ is the porosity.

Set $\mathbf{u} = (\mathbf{u}^s, \mathbf{u}^f)$ and let $\boldsymbol{\sigma}(\mathbf{u})$ and $p_f(\mathbf{u})$ denote the time Fourier transform of the total stress and the fluid pressure, respectively, and let $\mathbf{e}(\mathbf{u}^s)$ be the strain tensor of the solid phase. On each plane layer n in a sequence of N layers, the frequency-domain stress-strain relations are [17]

$$\sigma_{kl}(\mathbf{u}) = 2\mu e_{kl}(\mathbf{u}^s) + \delta_{kl} \left(\lambda_G \nabla \cdot \mathbf{u}^s + \alpha M \nabla \cdot \mathbf{u}^f \right), \quad (1)$$

$$p_f(\mathbf{u}) = -\alpha M \nabla \cdot \mathbf{u}^s - M \nabla \cdot \mathbf{u}^f. \quad (2)$$

The coefficient μ is the shear modulus of the bulk material, considered to be equal to the shear modulus of the dry matrix. The other coefficients in (1)-(2) can be obtained from the relations [17]

$$\lambda_G = K_G - \frac{2}{3}\mu, \quad K_G = K_m + \alpha^2 M, \quad (3)$$

$$\alpha = 1 - \frac{K_m}{K_s}, \quad M = \left(\frac{\alpha - \phi}{K_s} + \frac{\phi}{K_f} \right)^{-1},$$

where K_s, K_m and K_f denote the bulk moduli of the solid grains, dry matrix and saturant fluid, respectively.

Denoting by $\omega = 2\pi f$ the angular frequency, Biot's equations of motion in the diffusive range, stated in the space-frequency domain, are

$$\nabla \cdot \boldsymbol{\sigma}(\mathbf{u}) = 0, \quad (4)$$

$$\frac{i\omega\eta}{\kappa} \mathbf{u}^f + \nabla p_f(\mathbf{u}) = 0, \quad (5)$$

where η is the fluid viscosity and κ is the frame permeability.

Let us consider x_1 and x_3 as the horizontal and vertical coordinates, respectively. Gelinsky and Shapiro [11] showed that the medium behaves as a TI medium with the vertical symmetry axis at long wavelengths. They obtained the relaxed and unrelaxed limits, i.e., the low- and high-frequency limit real-valued stiffnesses, respectively. At all frequencies, the medium behaves as an equivalent TIV medium with complex and frequency-dependent stiffnesses, p_{IJ} , $I, J = 1, \dots, 6$. For the case of flow normal to the fracture layering and independent of the loading direction, these complex stiffnesses can be determined as presented by Krzikalla and Müller in [12] and Carcione et al. [13].

Denoting by $\boldsymbol{\tau}$ the stress tensor of the equivalent TIV medium and by $\boldsymbol{\varepsilon}$ the solid strain tensor at the macroscale, the corresponding stress-strain relations,

stated in the space-frequency domain, are [18,17]

$$\tau_{11}(u) = p_{11} \varepsilon_{11}(u^s) + p_{12} \varepsilon_{22}(u^s) + p_{13} \varepsilon_{33}(u^s), \quad (6)$$

$$\tau_{22}(u) = p_{12} \varepsilon_{11}(u^s) + p_{11} \varepsilon_{22}(u^s) + p_{13} \varepsilon_{33}(u^s), \quad (7)$$

$$\tau_{33}(u) = p_{13} \varepsilon_{11}(u^s) + p_{13} \varepsilon_{22}(u^s) + p_{33} \varepsilon_{33}(u^s), \quad (8)$$

$$\tau_{23}(u) = 2 p_{55} \varepsilon_{23}(u^s), \quad (9)$$

$$\tau_{13}(u) = 2 p_{55} \varepsilon_{13}(u^s), \quad (10)$$

$$\tau_{12}(u) = 2 p_{66} \varepsilon_{12}(u^s). \quad (11)$$

Here, we have assumed a closed system, for which the variation of fluid content $\zeta = -\nabla \cdot \mathbf{u}^f$ is equal to zero. This formulation provides the complex velocities of the fast modes at the macroscale and takes into account interlayer flow effects.

The coefficients p_{IJ} in (6)-(11) can be determined by applying five compressibility and shear harmonic FE tests to a representative 2D sample of the fractured poroelastic material. These tests are associated with boundary value problems for Biot's equations (4) stated in the space-frequency domain. The different boundary conditions represent the following virtual experiments [13]:

- (1) A compressibility test in the parallel direction to the fracture layering to determine p_{11} .
- (2) A compressibility test in the normal directions to the fracture layering to determine p_{33} .
- (3) A test applying simultaneous compressions in both, the normal and parallel directions to the fracture layering to determine p_{13} .
- (4) A shear test applied in the (x_1, x_3) -plane to determine p_{55} .
- (5) A shear test in the (x_1, x_2) plane to determine p_{66} .

Regarding the spatial discretization, the computational domain was partitioned uniformly into square cells of side length h . The FE spaces employed to represent each component of the solid displacement vector \mathbf{u}^s are locally bilinear functions which are globally continuous. The local degrees of freedom (DOF's) are the values of the components of \mathbf{u}^s at the four corners of the computational cells.

On the other hand, the relative fluid displacement \mathbf{u}^f was represented using the vector part of the Raviart-Thomas FE space of zero order [19]. The local DOF's are the values of the normal component of \mathbf{u}^f at the mid points of the faces of the computational cells.

The arguments presented in [15] can be applied here to show that the error of the FE procedure is of the order of $h^{1/2}$ in the energy norm and of the order h in the L^2 -norm.

For a detailed description of the FE tests used in this work, we refer to [13], where the model for these stiffnesses proposed by [12] was employed to validate the procedure.

The complex velocities of the equivalent TIV anisotropic medium are [17]

$$\begin{aligned} v_{\text{qP}} &= (2\bar{\rho})^{-1/2} \sqrt{p_{11}l_1^2 + p_{33}l_3^2 + p_{55} + A}, \\ v_{\text{qSV}} &= (2\bar{\rho})^{-1/2} \sqrt{p_{11}l_1^2 + p_{33}l_3^2 + p_{55} - A}, \\ v_{\text{SH}} &= \bar{\rho}^{-1/2} \sqrt{p_{66}l_1^2 + p_{55}l_3^2}, \\ A &= \sqrt{[(p_{11} - p_{55})l_1^2 + (p_{55} - p_{33})l_3^2]^2 + 4[(p_{13} + p_{55})l_1l_3]^2}, \end{aligned}$$

where $\bar{\rho} = \langle \rho \rangle$ is the thickness weighted average of the bulk density, $l_1 = \sin \theta$ and $l_3 = \cos \theta$ are the directions cosines, θ is the propagation angle between the wavenumber vector and the x_3 -symmetry axis and the three velocities correspond to the qP, qS and SH waves, respectively. The seismic phase velocity and quality factors are given by

$$v_p = \left[\text{Re} \left(\frac{1}{v} \right) \right]^{-1} \quad \text{and} \quad Q = \frac{\text{Re}(v^2)}{\text{Im}(v^2)}, \quad (12)$$

where v represents either v_{qP} , v_{qSV} or v_{SH} .

The energy-velocity vector \mathbf{v}_e of the qP and qSV waves is

$$\frac{\mathbf{v}_e}{v_p} = (l_1 + l_3 \cot \psi)^{-1} \hat{\mathbf{e}}_1 + (l_1 \tan \psi + l_3)^{-1} \hat{\mathbf{e}}_3, \quad (13)$$

with ψ being the angle between the energy-velocity vector and the x_3 -axis [17], while the energy velocity of the SH wave is [17]

$$\mathbf{v}_e = \frac{1}{\bar{\rho}v_p} (l_1 p_{66} \hat{\mathbf{e}}_1 + l_3 p_{55} \hat{\mathbf{e}}_3). \quad (14)$$

3 Numerical Results

The FE procedures described above were implemented in FORTRAN language and run in the SUN workstations of the Department of Mathematics at Purdue University. This approach yields the five complex stiffnesses p_{IJ} as a function of frequency and the corresponding phase velocities and dissipation coefficients. For each frequency, the five discrete problems associated with the harmonic compressibility and shear tests were solved using a public domain sparse matrix solver package. This approach yields directly the

frequency dependent velocities and dissipation coefficients, instead of solving Biot's equation in the space-time domain and using Fourier transforms to obtain the desired frequency domain characterization at the macroscale.

In all the experiments the numerical samples were discretized using a 160×160 uniform mesh representing 10 periods of 15 cm background sandstone and 1 cm fracture thickness. Both background and fractures have grain density $\rho_s = 2650 \text{ kg/m}^3$, bulk modulus $K_s = 37 \text{ GPa}$ and shear modulus $\mu_s = 44 \text{ GPa}$.

The dry bulk and shear modulus of the samples were determined using the Krief model [20],

$$\frac{K_m}{K_s} = \frac{\mu}{\mu_s} = (1 - \phi)^{3/(1-\phi)}. \quad (15)$$

A set of numerical examples consider the following cases:

- Case 1: A brine-saturated sample with fractures.
- Case 2: A brine-CO₂ patchy saturated sample without fractures.
- Case 3: A brine-CO₂ patchy saturated sample with fractures.
- Case 4: A brine saturated sample with a fractal frame and fractures.

Porosity is $\phi = 0.25$ in the background and $\phi = 0.5$ in the fractures. Using (15) we obtained $K_m = 1.17 \text{ GPa}$ and $\mu = 1.4 \text{ GPa}$ for the background and $K_m = 0.58 \text{ GPa}$ and $\mu = 0.68 \text{ GPa}$ for the fractures.

Permeability is obtained as [21]

$$\kappa = \frac{r_g^2 \phi^3}{45(1 - \phi)^2} \quad (16)$$

where $r_g = 20 \text{ }\mu\text{m}$ is the average radius of the grains.

Although the algorithm has already been validated in [13], we include, for completeness, a comparison of the analytical and numerical solutions for case 1. Figures 1 and 2 show plots of the dissipation factors and energy velocities of qP and qSV waves at 300 Hz, respectively, where it can be observed a very good match between the theoretical and numerical results.

<< Figure 1 >>

<< Figure 2 >>

Figures 3 and 4 show plots of the dissipation factors at 50 Hz and 300 Hz, for the cases 1, 2 and 3, while Figures 5 and 6 display the corresponding polar plots of the qP energy velocity. Loss is negligible in case 1 along the direction of the fracture plane. It can be observed strong velocity and Q anisotropy, with higher attenuation at 300 Hz and patchy brine-CO₂ saturation. Energy losses are much higher for angles between 60 and 90 degrees, i.e., for waves traveling in the direction incident normal to the fracture layering.

On the other hand, velocity anisotropy caused by the fractures in cases 1 and 3 is enhanced for the case of patchy saturation, with lower velocities when patches are present. The velocity behaves isotropically in case 2.

<< Figure 3 >>

<< Figure 4 >>

<< Figure 5 >>

<< Figure 6 >>

Figures 7 and 8 show the fluid pressure distribution at frequencies 50 Hz

and 300 Hz, respectively, for case 3 and compressions normal to the fracture layering. It can be observed that pressure gradients take their highest values at the fractures, and at 300 Hz remain always higher than at 50 Hz. This explains the higher losses for qP waves at 300 Hz as compared with the 50 Hz experiment observed in Figures 3 and 4.

<< Figure 7 >>

<< Figure 8 >>

Denoting by Q_{P1} , Q_{P2} and Q_{P3} the qP-quality factors associated with cases 1, 2 and 3, Figure 9 shows the approximate validity of the commonly used approximation for the dissipation factors for qP waves

$$Q_{P3}^{-1} = Q_{P1}^{-1} + Q_{P2}^{-1} \tag{17}$$

relating different attenuation mechanisms for these cases at 300 Hz as function of the propagation angle. This approximation was also tested in [22] and [23]. Numerical experiments have shown that this equation cannot be used as an approximation in Case 4.

<< Figure 9 >>

Figures 10 and 11 show polar plots of the dissipation factors of qSV waves at 50 Hz and 300 Hz, respectively, for the three cases. For both frequencies, case 2 shows isotropic attenuation, while for a fractured sample brine or patchy saturated (cases 1 and 3), Q anisotropy is strong for angles between 30 and

60 degrees, with about a 50 % increase in attenuation at 300 Hz with respect to 50 Hz.

<< Figure 10 >>

<< Figure 11 >>

Figure 12 displays polar plots of the qSV energy velocities at 50 Hz, where velocity anisotropy is observed to be induced by fractures (cases 1 and 3), while patchy saturation , as expected, does not affect the anisotropic behavior of the qSV velocities. On the other hand, case 2 shows isotropic velocity, with higher velocity values than for the fractured cases. The corresponding qSV energy velocities at 300 Hz are almost identical to those at 50 Hz and are not shown.

Figure 13 displays polar plots of the SH-wave energy velocity at 50 Hz, where velocity is observed to be induced by fractures. Cases 1 and 3 are almost indistinguishable, while the velocity for case 2 is isotropic. SH energy velocities at 300 Hz are identical to those 50 Hz, since there is no energy loss (p_{55} and p_{66} are real [9]).

<< Figure 12 >>

<< Figure 13 >>

Figures 14 and 15 analyze the variations in attenuation of qP waves for case 3

due to changes in CO₂ saturation, with attenuation coefficients computed at 300 Hz. Figure 14 shows that an increase of CO₂ saturation from 10% to 50% induces a noticeable decrease in attenuation for angles close to the normal orientation of the fractures. Figure 15 displays the corresponding attenuation curves for qSV waves, where the same decrease in attenuation is observed, but for angles between 30 and 60 degrees.

<< Figure 14 >>

<< Figure 15 >>

On the other hand, it was observed that qP energy velocities decrease for increasing CO₂ saturation, with the greater decreases for angles closer to the normal layering of the fractures. For qSV and SH waves, energy velocities show almost no change between the two CO₂ saturations. The related plots are omitted for brevity.

Next, we analyze the behavior of waves as a function of frequency in the range 1 Hz - 1 kHz at 10% CO₂ saturation. Figures 16 and 17 display dissipation factors for cases 1, 2 and 3 for waves parallel ('11' waves) and normal ('33' waves) to the fracture layering, respectively, while Figures 18 and 19 show the corresponding velocities.

Figure 16 indicate that '11' waves for case 1 (brine-saturated homogeneous background with fractures) are lossless, while the cases of patchy saturation with and without fractures suffer similar attenuation, though there is a change from lower to higher attenuation for the patchy saturated case with fractures (case 3) at a frequency of about 40 Hz.

On the other hand, the curves for '33' waves displayed in Figure 17 show much higher attenuation than those for '11' waves for the three cases. The case of patchy saturation with fractures (case 3) is the one exhibiting the highest attenuation values for all frequencies. Besides, the case of brine-saturated homogeneous background with fractures (case 1) shows a much higher attenuation than the non-fractured patchy saturated case (case 2) starting at a frequency

of about 26 Hz, while below such frequency the opposite behavior is observed, though with quite similar attenuation.

<< Figure 16 >>

<< Figure 17 >>

Figure 18 shows that for the case of brine-saturated homogeneous background with fractures (case 1), ‘11’ velocities are essentially independent of frequency. In the case of patchy saturation with fractures (case 3), velocities are always smaller than in case 1, i.e., the presence of CO₂ patches induces a velocity decay in the whole range of frequencies analyzed. On the other hand, velocities for patchy saturation with or without fractures show a similar increasing behavior with frequency.

Figure 19 shows that ‘33’ waves have the higher frequency dependent behavior for the case of a patchy saturated fractured medium (case 3), with lower values than in the other two cases and increasing behavior after 10 Hz. When the sample is brine saturated with fractures (case 1), velocities are higher than in case 3 . On the other hand, the patchy saturated case without fractures exhibits the highest velocity values with moderate increase with frequency. Thus, for ‘33’ waves the presence of fractures induces a noticeable reduction of velocities normal to the fracture plane, either for brine or patchy saturation.

<< Figure 18 >>

<< Figure 19 >>

The last experiment (case 4) analyzes the effects of the presence of heterogeneities in the skeleton or frame of the fractured sample. The binary fractal permeability is obtained with the following logarithmic relation [24,25]

$$\log \kappa(x, z) = \langle \log \kappa \rangle + f(x, z) \quad (18)$$

with $f(x, z)$ being the fractal representing the spatial fluctuation of the permeability field, chosen to be of fractal dimension $D = 2.2$, correlation length 2 cm and average permeability 0.25 Darcy in the background and 4.44 Darcy in the fractures. Porosity was obtained using the Kozeny-Carman relation. Thus, the heterogeneous sample was constructed as a fractal perturbation of the sample in case 1. Figure 20 shows the Lamé coefficient λ_G of the brine saturated fractal sample used in case 4.

<< Figure 20 >>

Figures 21 and 22 compare the qP and qSV dissipation factors of this case at 50 Hz with those of case 1, while Figures 23 and 24 compares the corresponding energy velocities. As in the patchy saturation case, frame heterogeneities induce a noticeable increase in Q anisotropy for qP waves for angles normal to the fracture plane and for qSV waves for angles between 30 and 60 degrees. From Figures 21 and 22, we conclude that qSV wave attenuation is more affected than qP attenuation when frame heterogeneities are present. Also, from Figures 23 and 24 we see the expected energy velocity reduction in the heterogeneous case, and that velocity anisotropy is less affected by frame heterogeneities than Q anisotropy. Concerning SH velocities, they show anisotropy and a moderate reduction in velocity and negligible attenuation in the heterogeneous case. The SH energy velocity is similar to that in case 1 of Figure 11 and the plot is omitted.

<< Figure 21 >>

<< Figure 22 >>

<< Figure 23 >>

<< Figure 24 >>

4 Conclusions

We have presented a set of numerical quasi-static harmonic experiments to determine the complex and frequency dependent stiffnesses of a viscoelastic transversely isotropic homogeneous medium equivalent to a fluid-saturated poroelastic material containing a dense set of planar fractures. The numerical simulators are based on the finite-element solution of Biot's equations in the diffusive range with boundary conditions representing compressibility and shear tests. The fractures are modeled as very thin highly permeable poroelastic layers of small frame moduli.

The numerical experiments consider brine, patchy brine-CO₂ saturation and fractal frame heterogeneities, with and without fractures. Attenuation, velocity dispersion and anisotropy are analyzed as a function of both propagation angle and frequency. The effects of variation in CO₂ saturation has also been analyzed.

Strong velocity and attenuation anisotropy can be observed in the qP and qSV wave modes, with attenuation enhanced when patches of CO₂ are present, and decreasing attenuation with increasing CO₂ patchy saturation. While the higher values of the dissipation factor for qP waves are found to be at angles close to the normal direction to the fracture layering, for qSV waves the higher values are found at angles between 30 and 60 degrees. Both, qP and qSV waves, show a decrease in velocity when fractures are present, and Q anisotropy is more pronounced than velocity anisotropy.

There is no shear loss in the absence of fractures, since the attenuation mechanism is only affecting the P waves. Fractures induce anisotropy and the P-S coupling generates losses in the shear waves as well.

On the other hand, the horizontally polarized S-wave (the SH wave) is lossless because it is a pure mode in transversely isotropic media, although exhibits velocity anisotropy, as expected.

The analysis of waves traveling parallel ('11') and normal ('33') to the fracture plane as a function of frequency has been performed in the range 1 Hz-1 kHz. It has been observed lower dissipation factors for '11' than for '33' waves, as expected, and the attenuation peak for '11' waves at a lower frequency than that for '33' waves.

Regarding the velocities, '11' waves show a stronger dependency on frequency as compared with '33' waves, and the presence of fractures induces a noticeable reduction in velocities in all the frequency range analyzed for '33' waves and at low frequencies up to about 90 Hz for '11' waves.

In the last experiment, based on frame heterogeneities, it has been observed a similar effect on velocity and Q anisotropy than in the patchy saturation case, with enhanced Q anisotropy and energy velocity reduction in all waves, being the qSV waves the more affected by the fractal variations of the porous frame.

5 Acknowledgements

The work of J. E. Santos was partially funded by the GRANT PIP 112-20080100952 from CONICET, Argentina. The authors wish to thank Robert McGraw and J. Chapman Flack of the Computing Systems at Purdue University for their technical support in running the numerical experiments. J. M. Carcione has been partially funded by the CO2Monitor project.

References

- [1] Schoenberg, M., and Douma, J., Elastic wave propagation in media with parallel fractures and aligned cracks, *Geophys. Prosp.*, 36, 571-590, 1988.
- [2] Gurevich, B., Elastic properties of saturated porous rocks with aligned fractures, *J. Appl. Geophys.*, 54, 203-218, 2003
- [3] Grechka, V., Comparison of the non-interaction and differential schemes in predicting the effective elastic properties of fractured media: *International J. of Fracture*, 144, 181-188, 2007.
- [4] Picotti, S., Carcione, J. M., Gei, D., Rossi, G., and Santos, J. E., Seismic modeling to monitoring CO₂ geological storage. The Atzbach-Schwanenstadt gas field, *J. Geophys. Res.*, 117, B06103, 2012.
- [5] Grechka, V., and Kachanov, M., Effective elasticity of rocks with closely spaced and intersecting cracks: *Geophysics*, 71, D85-D91, 2006.
- [6] Grechka, V., and Kachanov, M., 2006, Effective elasticity of fractured rocks: A snapshot of the work in progress: *Geophysics*, 71, W45-W58, 2006.
- [7] Saenger E. H., Ciz, R., O. S. Krüger, O. S., Schmalholz, S. M., Gurevich, B., and Shapiro, S. A., Finite-difference modeling of wave propagation on microscale: A snapshot of the work in progress, *Geophysics*, 72, SM293-SM300, 2007.
- [8] Wenzlau, F., Altmann, J. B., and Müller, T. M., Anisotropic dispersion and attenuation due to wave-induced flow: quasi-static finite element modeling in poroelastic solids, *J. Geophys. Res.*, 115, B07204, doi:10.1029/2009JB006644, 2010.
- [9] Carcione, J. M., Gurevich, B., and Santos, J. E., and Picotti, S., Angular and frequency dependent wave velocity and attenuation in fractured porous media, *Pure Appl. Geophys.*, DOI 10.1007/s00024-012-0636-8, 2013.
- [10] White, J. E., Mikhaylova, N. G., and Lyakhovitskiy, F. M., Low-frequency seismic waves in fluid saturated layered rocks, *Physics of the Solid Earth*, 11, 654-659, 1975.
- [11] Gelinsky, S., and Shapiro, S. A., Poroelastic Backus-averaging for anisotropic, layered fluid and gas saturated sediments, *Geophysics*, 62, 1867-1878, 1997.
- [12] Krzikalla, F. and Müller, T., Anisotropic P-SV-wave dispersion and attenuation due to interlayer flow in thinly layered porous rocks, *Geophysics*, 76, W 135; doi:10.1190/1.3555077, 2011.
- [13] Carcione, J. M., Santos, J. E. and Picotti, S., Anisotropic poroelasticity and wave-induced fluid flow. Harmonic finite-element simulation, *Geophys. J. Internat.*, 186, 1245-1254, 2011.

- [14] Picotti, S., and Carcione, J. M., Santos, J. E., and Gei, D., Q-anisotropy in finely-layered media, *Geophys. Res. Lett.*, 37, L06302, 2010.
- [15] Santos, J. E., Rubino, J. G., and Ravazzoli, C. L., A numerical upscaling procedure to estimate effective bulk and shear moduli in heterogeneous fluid-saturated porous media, *Comput. Methods Appl. Mech. Engrg.*, 198, 2067-2077, 2009.
- [16] Santos, J. E., Carcione, J. M., and Picotti, S., Viscoelastic-stiffness tensor of anisotropic media from oscillatory numerical experiments, *Comput. Methods Appl. Mech. Engrg.*, 200, 896-904, 2011.
- [17] Carcione, J.M., 2007. Wave fields in real media: wave propagation in anisotropic, anelastic, porous and electromagnetic media, in *Handbook of Geophysical Exploration*, 2nd edn, Vol. 38, 515pp., eds Helbig, K. & Treitel, S., Elsevier, Oxford.
- [18] Carcione, J. M., Anisotropic Q and velocity dispersion of finely layered media. *Geophys. Prosp.*, 40, 761-783, 1992.
- [19] Raviart, P. A., and Thomas, J. M., Mixed finite element method for 2nd order elliptic problems, *Mathematical Aspects of the Finite Element Methods*, Lecture Notes of Mathematics, vol. 606, Springer, 1975.
- [20] Krief, M., Garat, J. Stellingwerff, J. and Ventre, J., A petrophysical interpretation using the velocities of P and S waves (full waveform sonic), *The Log Analyst*, 31, 355-369, 1990.
- [21] Carcione, J. M., Gurevich, B., and Cavallini, F., A generalized Biot-Gassmann model for the acoustic properties of shaley sandstones, *Geophys. Prosp.*, 48, 539-557, 2000.
- [22] Gurevich, B., Zyrianov, V. B, and Lopatnikov, S. L., Seismic attenuation in finely layered porous rocks: Effects of fluid flow and scattering, *Geophysics*, 62, 319-324, 1997.
- [23] Carcione, J. M., Santos, J. E., and Picotti, S., Fracture induced anisotropic attenuation, *Rock Mech. Rock Engrg.*, 45, 929-942, 2012.
- [24] Russo, D., and Bouton, M., Statistical analysis of spatial variability in unsaturated flow parameters, *Water Res. Res.*, 28, 1911-1925, 1992.
- [25] Russo, D., Russo, I., and Laufer, A., On the spatial variability of parameters of the unsaturated hydraulic conductivity, *Water Res. Res.*, 33, 945-956, 1997.

List of Figures

1	Dissipation factor of the qP and qSV waves at 300 Hz for case 1. The solid lines indicate the theoretical values.	20
2	Polar representation of the qP and qSV energy velocity vector at 300 Hz for case 1. The solid lines indicate the theoretical values.	20
3	Dissipation factor of the qP waves at 50 Hz for cases 1, 2 and 3 .	21
4	Dissipation factor of the qP waves at 300 Hz for cases 1, 2 and 3 .	21
5	Polar representation of the qP energy velocity vector at 50 Hz for cases 1, 2 and 3 .	22
6	Polar representation of the qP energy velocity vector at 300 Hz for cases 1, 2 and 3 .	22
7	Fluid pressure distribution at 50 Hz for the compressibility test for case 3 with compression normal to the fracture plane ('33')	23
8	Fluid pressure distribution at 300 Hz for the compressibility test for case 3 with compression normal to the fracture plane ('33')	23
9	Test of the approximate validity of equation (17) for cases 1, 2 and 3 at 300 Hz.	24
10	Dissipation factor of the qSV waves at 50 Hz for cases 1, 2 and 3 . The lossless case 3 is represented by a point at the origin	25
11	Dissipation factor of the qSV waves at 300 Hz for cases 1, 2 and 3 . The lossless case 3 is represented by a point at the origin	25
12	Polar representation of the qSV energy velocity vector at 50 Hz for cases 1, 2 and 3 .	26
13	Polar representation of the SH energy velocity vector at 50 Hz for cases 1, 2 and 3 .	26

14	Dissipation factor of qP waves for case 3 at 300 Hz for 10% and 50% CO ₂ saturation.	27
15	Dissipation factor of qSV waves for case 3 at 300 Hz for 10% and 50% CO ₂ saturation.	27
16	Dissipation factor of waves parallel to the fracture plane ('11' waves) as function of frequency	28
17	Dissipation factor factor of waves normal to the fracture plane ('33'waves) as function of frequency	28
18	Velocity of waves parallel to the fracture plane ('11' waves) as function of frequency	29
19	Velocity of waves normal to the fracture plane ('33'waves) as function of frequency	29
20	Lamé coefficient (GPa) for the brine-saturated fractal porosity-permeability sample of case 4.	30
21	Dissipation factor of qP waves at 50 Hz for a brine saturated homogeneous background with fractures (case 1) and a brine saturated fractal-porosity permeability background with fractures (case 4).	31
22	Dissipation factor of qSV waves at 50 Hz for a brine saturated homogeneous background with fractures (case 1) and a brine saturated fractal-porosity permeability background with fractures (case 4).	31
23	Polar representation of the qP energy velocity vector at 50 Hz for a brine saturated homogeneous background with fractures (case 1) and a brine saturated fractal-porosity permeability background with fractures (case 4).	32
24	Polar representation of the qSV energy velocity vector at 50 Hz for a brine saturated homogeneous background with fractures (case 1) and a brine saturated fractal-porosity permeability background with fractures (case 4).	32

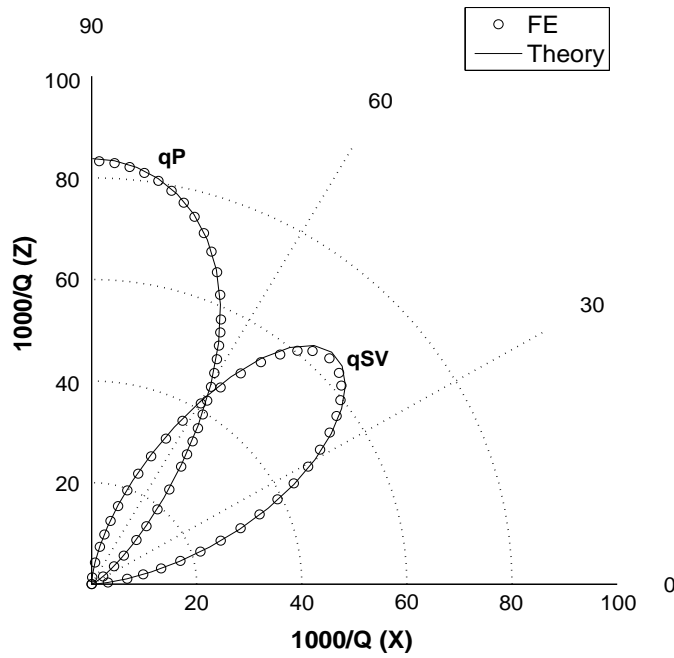


Fig. 1. Dissipation factor of the qP and qSV waves at 300 Hz for case 1. The solid lines indicate the theoretical values.

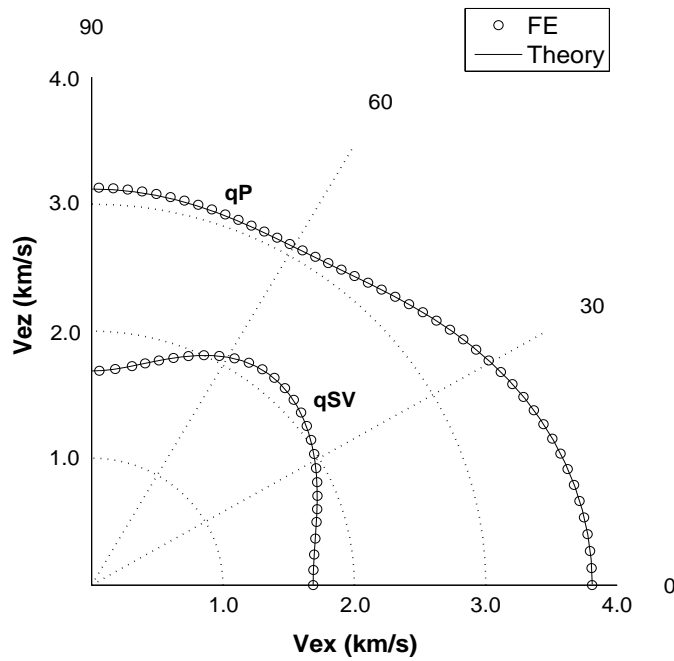


Fig. 2. Polar representation of the qP and qSV energy velocity vector at 300 Hz for case 1. The solid lines indicate the theoretical values.

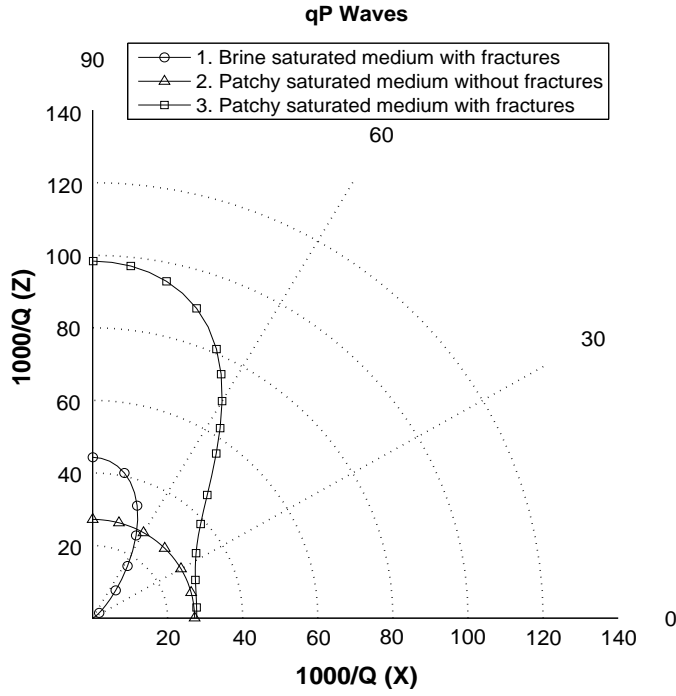


Fig. 3. Dissipation factor of the qP waves at 50 Hz for cases 1, 2 and 3 .

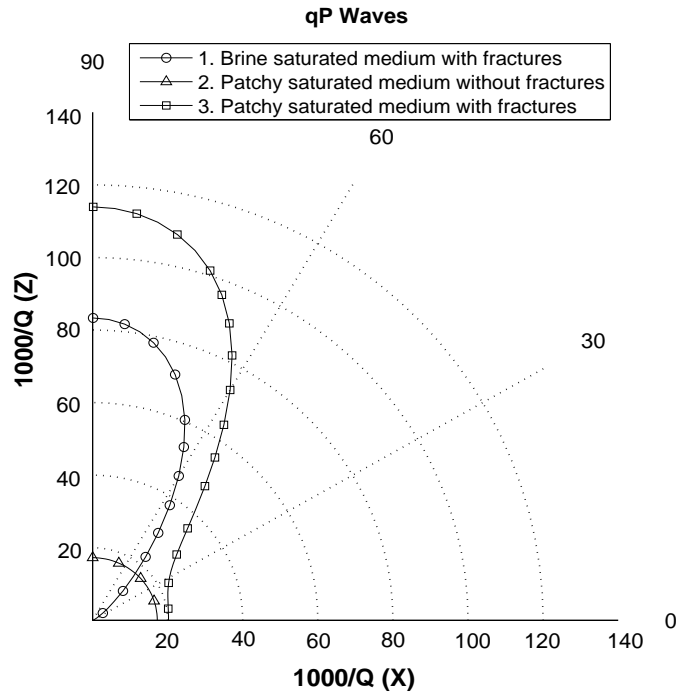


Fig. 4. Dissipation factor of the qP waves at 300 Hz for cases 1, 2 and 3 .

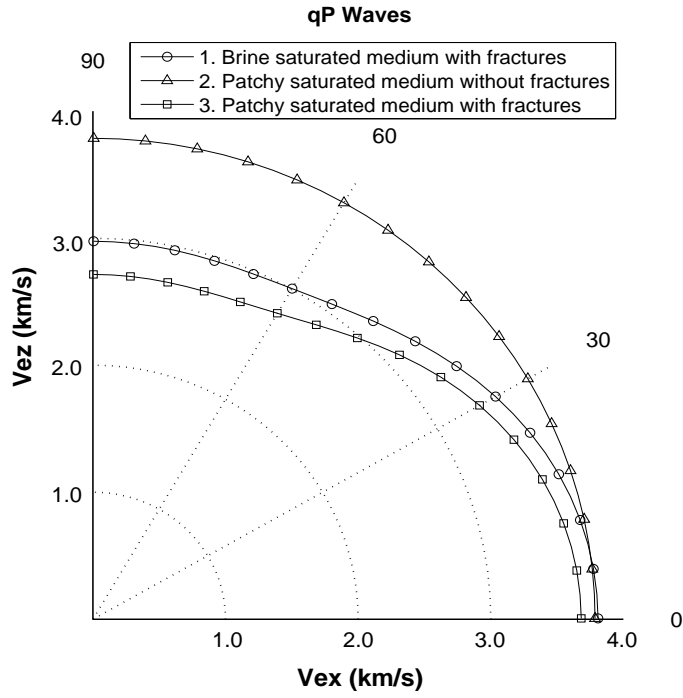


Fig. 5. Polar representation of the qP energy velocity vector at 50 Hz for cases 1, 2 and 3 .

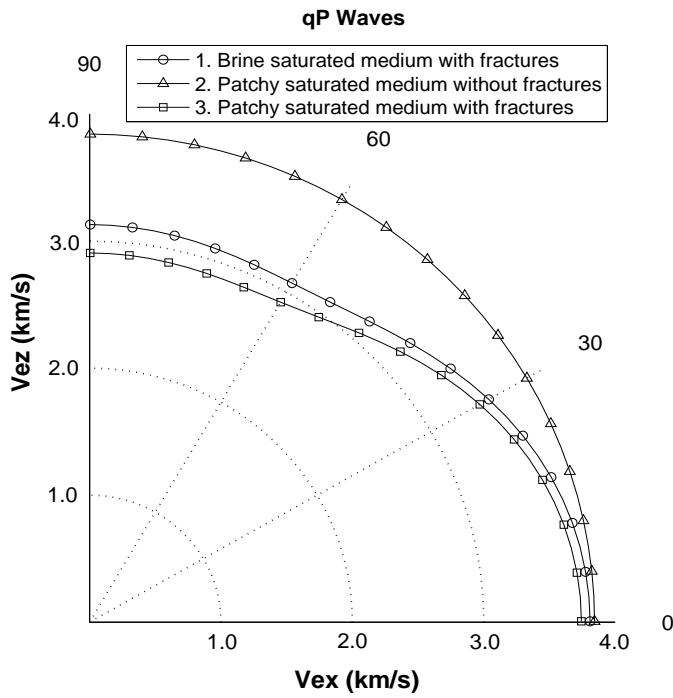


Fig. 6. Polar representation of the qP energy velocity vector at 300 Hz for cases 1, 2 and 3 .

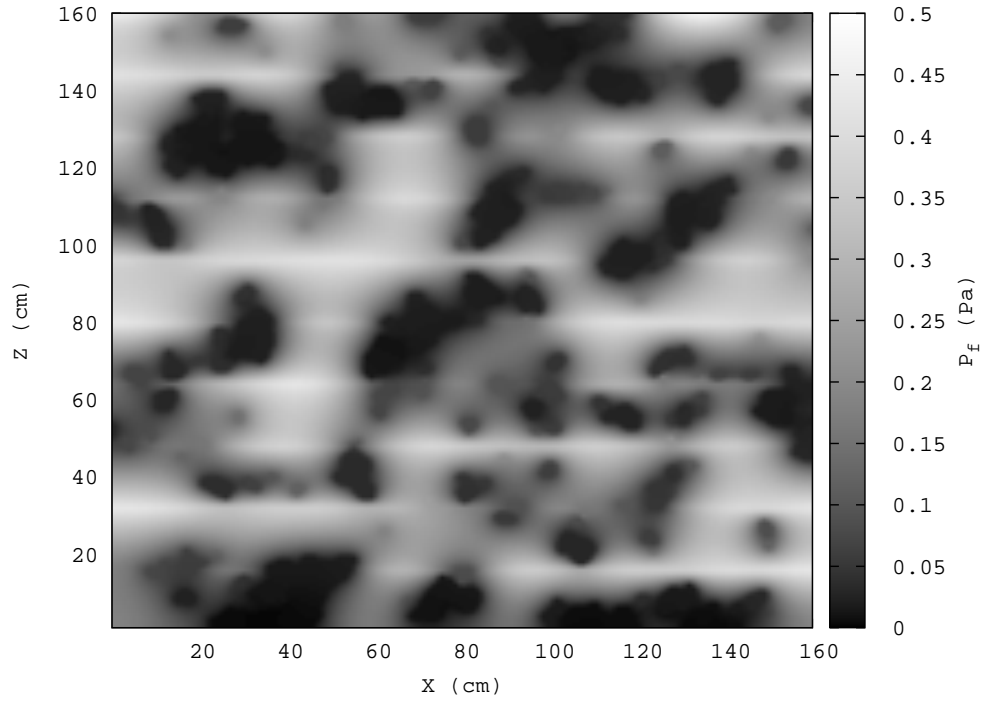


Fig. 7. Fluid pressure distribution at 50 Hz for the compressibility test for case 3 with compression normal to the fracture plane ('33')

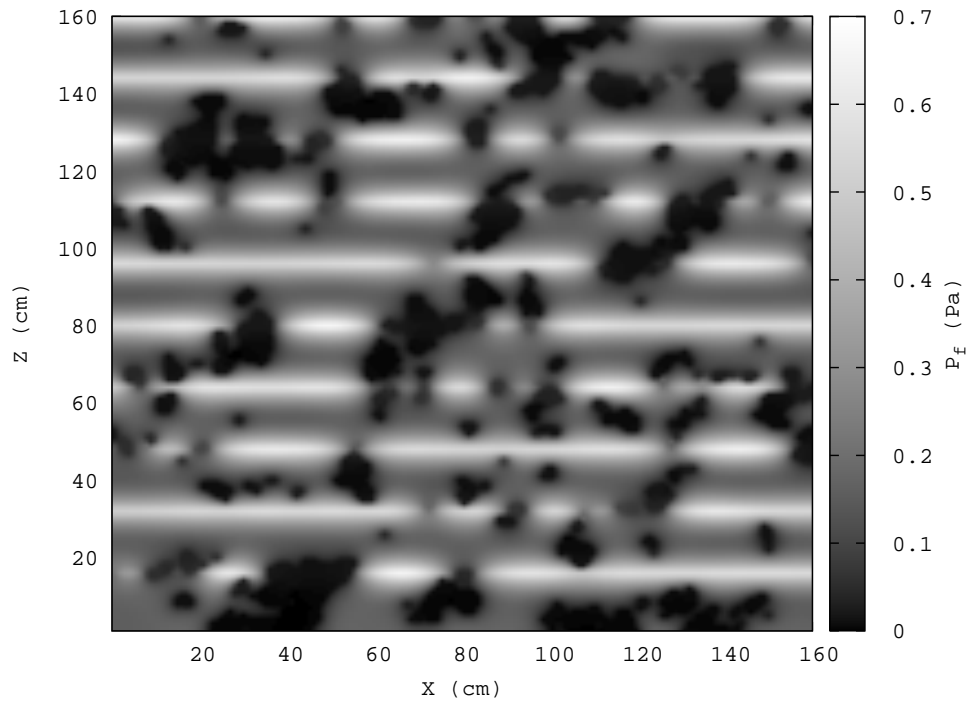


Fig. 8. Fluid pressure distribution at 300 Hz for the compressibility test for case 3 with compression normal to the fracture plane ('33')

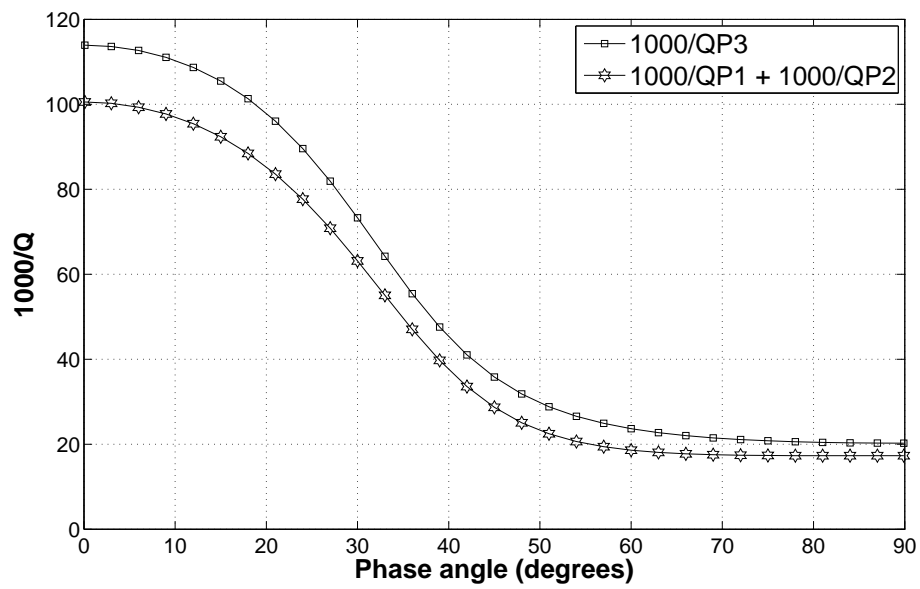


Fig. 9. Test of the approximate validity of equation (17) for cases 1, 2 and 3 at 300 Hz.

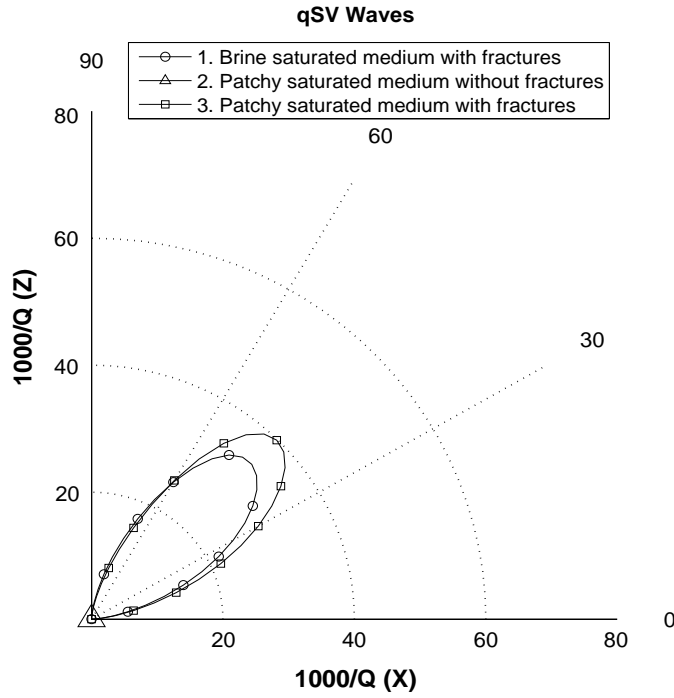


Fig. 10. Dissipation factor of the qSV waves at 50 Hz for cases 1, 2 and 3 . The lossless case 3 is represented by a point at the origin

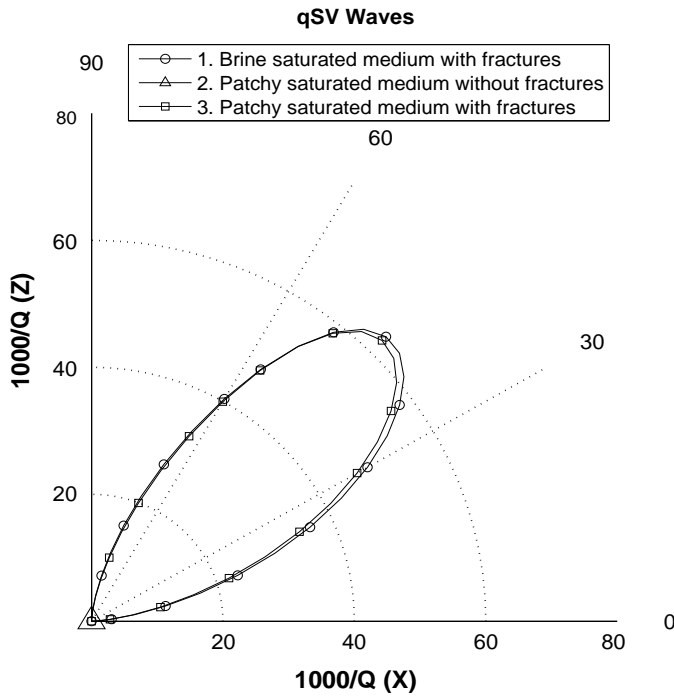


Fig. 11. Dissipation factor of the qSV waves at 300 Hz for cases 1, 2 and 3 . The lossless case 3 is represented by a point at the origin

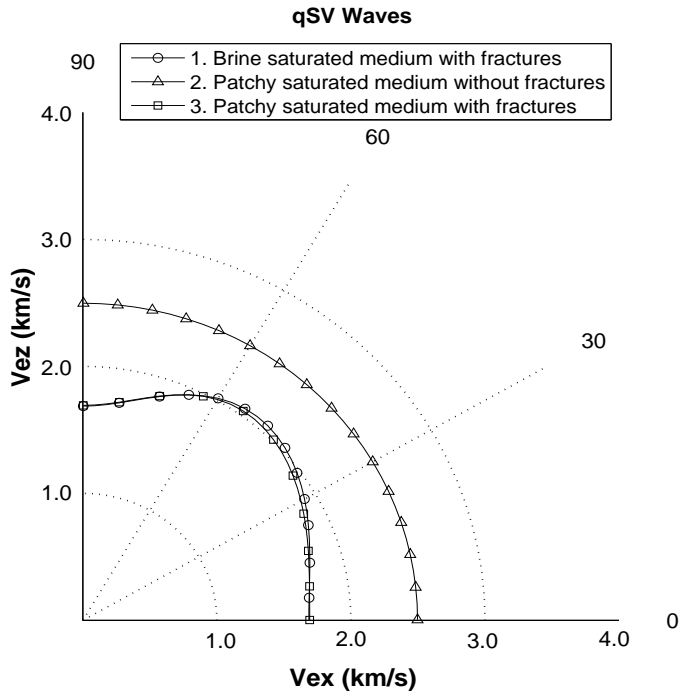


Fig. 12. Polar representation of the qSV energy velocity vector at 50 Hz for cases 1, 2 and 3 .

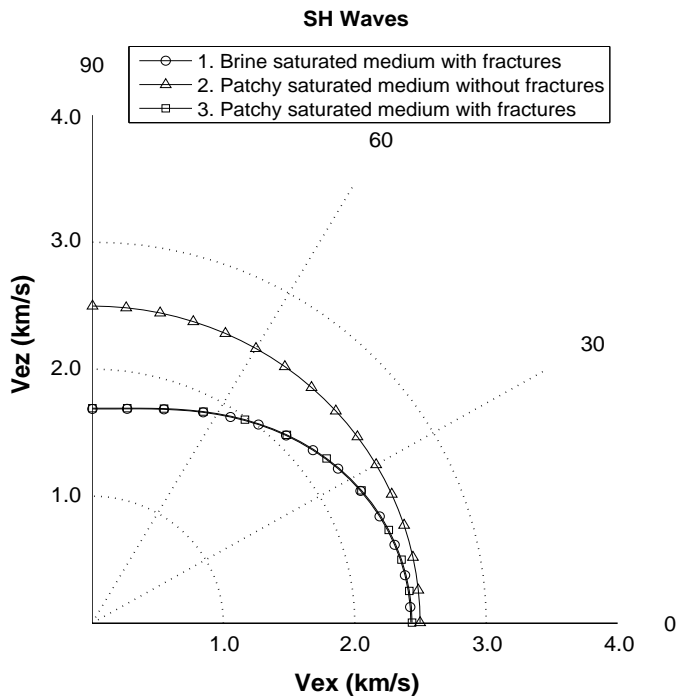


Fig. 13. Polar representation of the SH energy velocity vector at 50 Hz for cases 1, 2 and 3 .

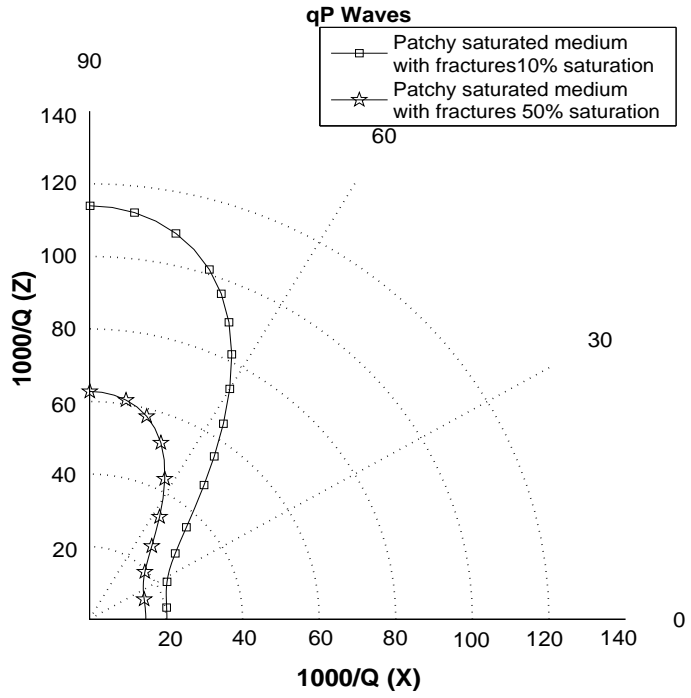


Fig. 14. Dissipation factor of qP waves for case 3 at 300 Hz for 10% and 50% CO₂ saturation.

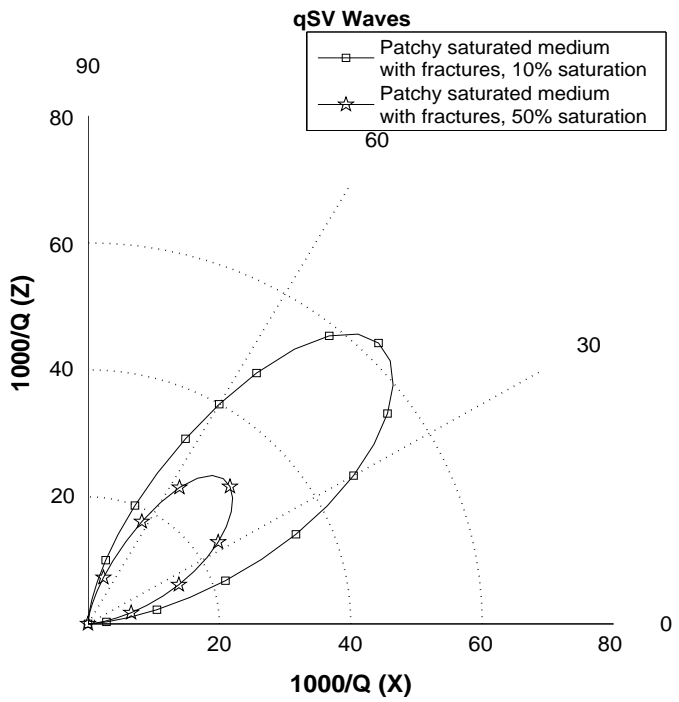


Fig. 15. Dissipation factor of qSV waves for case 3 at 300 Hz for 10% and 50% CO₂ saturation.

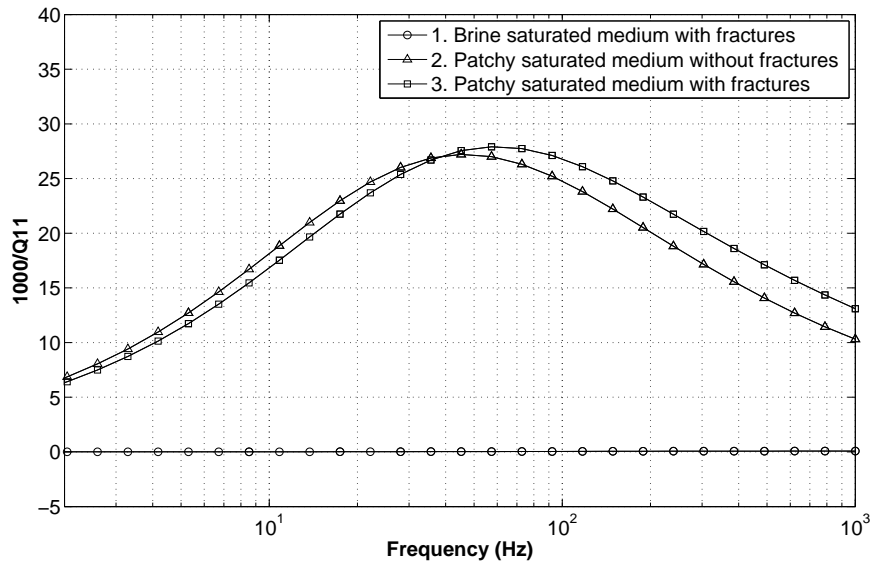


Fig. 16. Dissipation factor of waves parallel to the fracture plane ('11' waves) as function of frequency

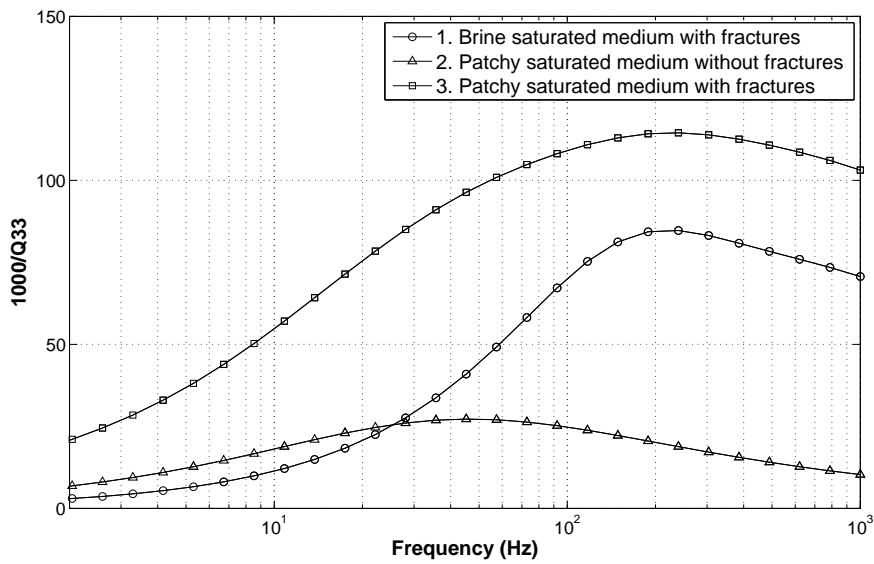


Fig. 17. Dissipation factor factor of waves normal to the fracture plane ('33' waves) as function of frequency

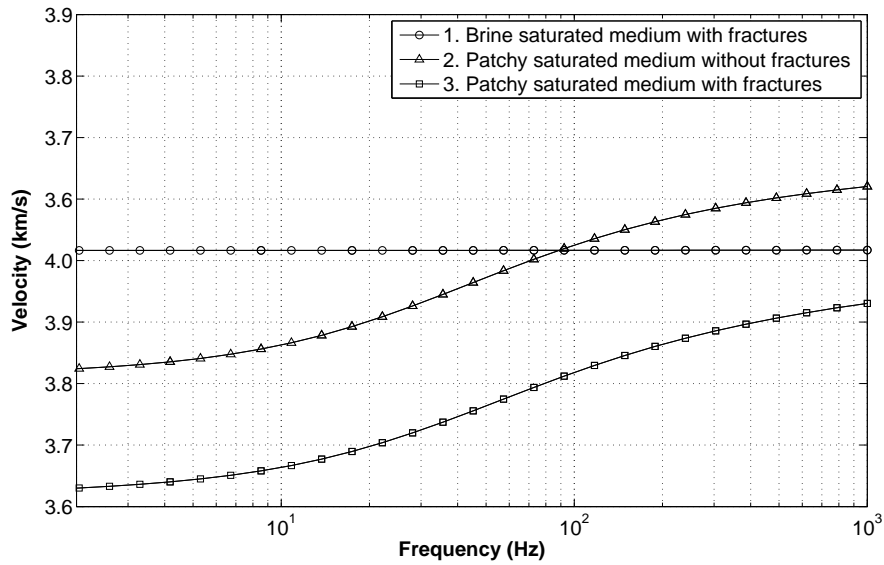


Fig. 18. Velocity of waves parallel to the fracture plane ('11' waves) as function of frequency

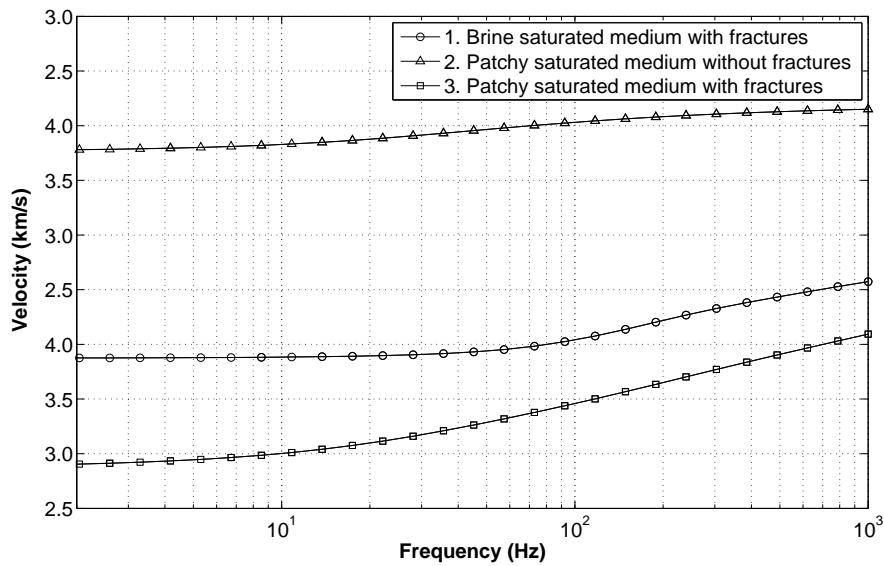


Fig. 19. Velocity of waves normal to the fracture plane ('33' waves) as function of frequency

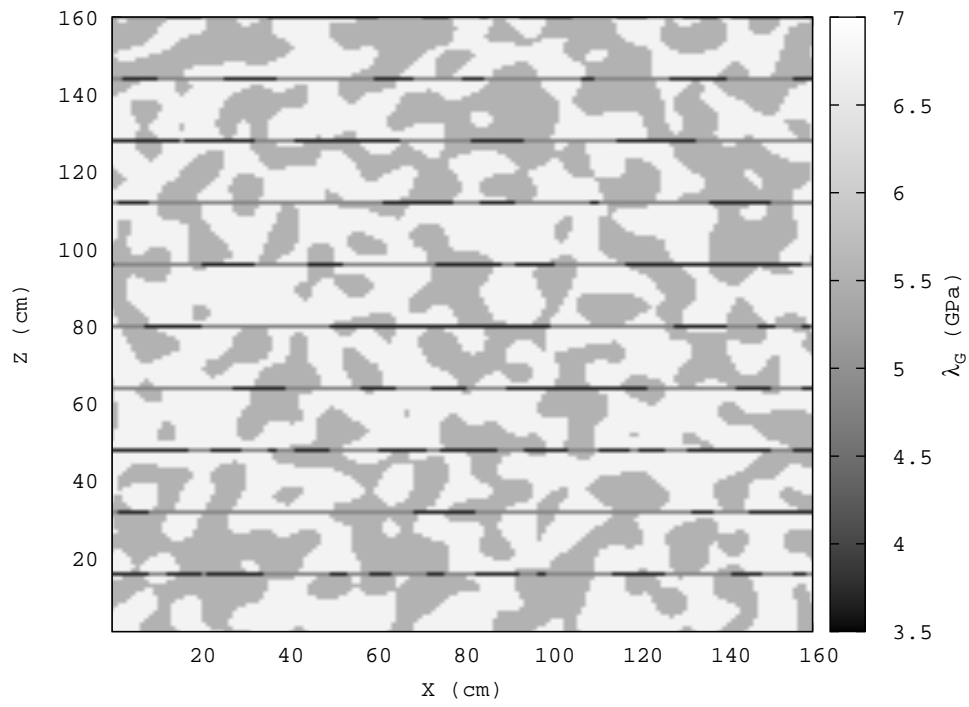


Fig. 20. Lamé coefficient (GPa) for the brine-saturated fractal porosity-permeability sample of case 4.

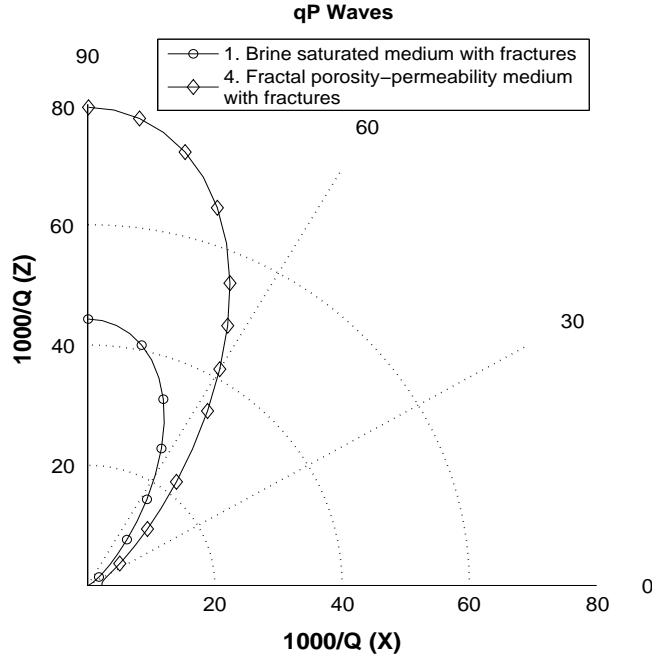


Fig. 21. Dissipation factor of qP waves at 50 Hz for a brine saturated homogeneous background with fractures (case 1) and a brine saturated fractal-porosity permeability background with fractures (case 4).

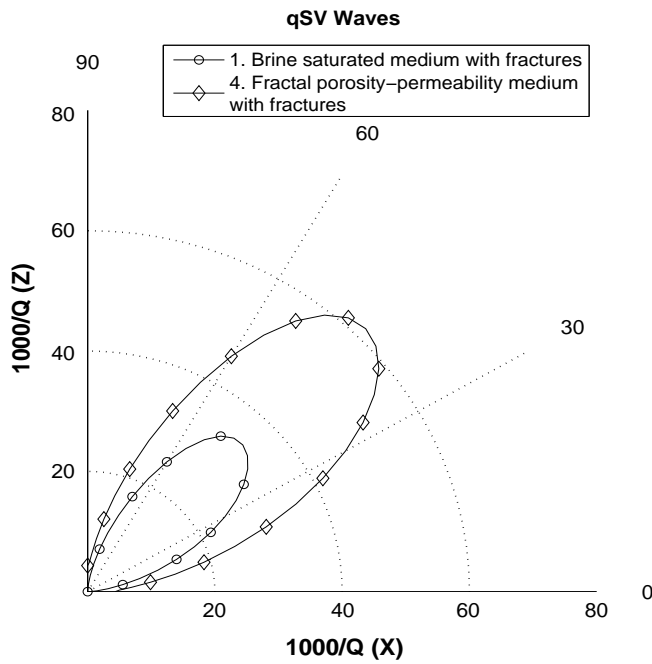


Fig. 22. Dissipation factor of qSV waves at 50 Hz for a brine saturated homogeneous background with fractures (case 1) and a brine saturated fractal-porosity permeability background with fractures (case 4).

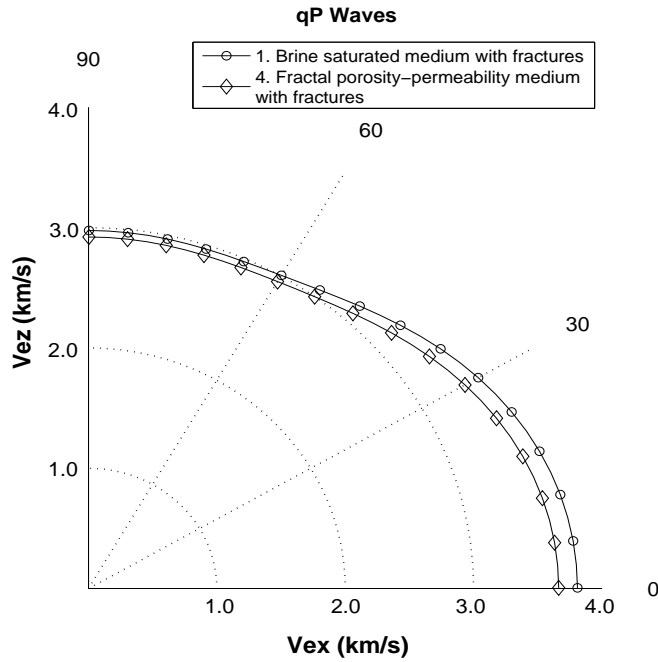


Fig. 23. Polar representation of the qP energy velocity vector at 50 Hz for a brine saturated homogeneous background with fractures (case 1) and a brine saturated fractal-porosity permeability background with fractures (case 4).

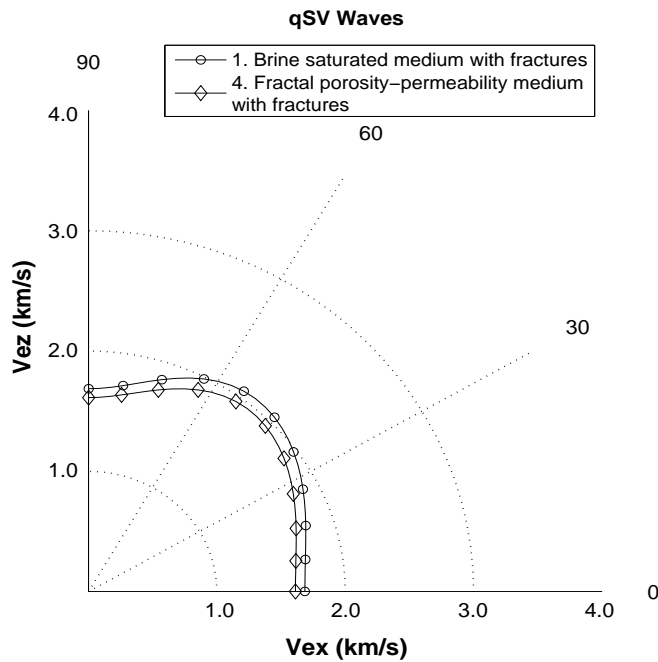


Fig. 24. Polar representation of the qSV energy velocity vector at 50 Hz for a brine saturated homogeneous background with fractures (case 1) and a brine saturated fractal-porosity permeability background with fractures (case 4).